Optimisation of a corrugation-pitch-modulated DFB laser structure with inhomogeneous coupling coefficient for stable single longitudinal mode operation

J.B.M. Boavida, J.A.P. Morgado, C.A.F. Fernandes

EPJ manuscript No.
(will be inserted by the editor)

Optimisation of a Corrugation-Pitch-Modulated DFB Laser Structure with Inhomogeneous Coupling Coefficient for Stable Single Longitudinal Mode Operation

José B. M. Boavida[1], José A. P. Morgado[2], and Carlos A. F. Fernandes[3]

[1] Optical Communications Group, Instituto de Telecomunicações, Av. Rovisco Pais, 1049–001 Lisboa, Portugal, (e-mail: jose.boavida@gmail.com).
[2] Optical Communications Group, Instituto de Telecomunicações, Av. Rovisco Pais, 1049–001 Lisboa, Portugal, and also Portuguese Air Force Academy, Granja do Marquês, 2715-021 Sintra, Portugal (e-mail: japmorgado@gmail.com).
[3] Optical Communications Group, Instituto de Telecomunicações, Av. Rovisco Pais, 1049–001 Lisboa, Portugal (e-mail: ffernandes@ist.utl.pt).

Received: date / Revised version: date

Abstract. This paper shows that a suitable design of a corrugation-pitch-modulated (CPM) distributed-coupling-coefficient (DCC) distributed feedback (DFB) laser structure can strongly improve the mode selectivity ($\mathfrak{S}$) and the flatness ($\mathfrak{F}$) of DFB laser structures in order to ensure the required criteria for single longitudinal mode operation ($\mathfrak{S} \geq 0.25$ and $\mathfrak{F} \leq 0.05$), through an extended range of current injection. It is shown that a symmetric structure should be used in order to accomplish the requirements imposed by the modern optical communication systems. Photon and carrier rate equations have been used in order to evaluate the performance of the proposed laser structure in the above threshold regime. The variations of $\mathfrak{S}$, $\mathfrak{F}$, the lasing wavelength, the emitted power (P) and the side-mode-suppression-ratio (SMSR) with the current injection (I) have been evaluated. For $I = 5\,I_{th}$, where I_{th} is the laser threshold current, substantial improvements in $\mathfrak{S}$ (3.8 times better), in $\mathfrak{F}$ (2 times better), in P (15 % higher) and in the SMSR (about 3.4 dB higher) are achieved in the proposed CPM-DCC-DFB laser when compared to an optimised CPM-DCC-DFB laser referred elsewhere. The improvements are even better when compared to the standard QWS-DFB laser.

PACS. 42.55.Px Semiconductor lasers; laser diodes – 85.60.-q Optoelectronic devices – 42.82.-m Integrated optics – 75.40.-Mg Numerical simulations studies

1 Introduction

Non-conventional distributed feedback (DFB) laser diodes have been successively proposed to be used in optical communication systems (OCS) as improved alternatives to the quarterly wavelength-shifted (QWS)-DFB laser diode. These lasers aim to avoid the degradation of single longitudinal mode (SLM) operation with the current injection, by reducing the spatial hole-burning (SHB) effect [1, p. 159], [2, p. 249], [3, p. 123]. This reduction can be achieved by optimising the coupling coefficient profile [3, pp. 136–141] and/or modulating the corrugation pitch [4] along the cavity length. While the first option aims mainly at enlarging the laser selectivity ($\mathfrak{S}$), the second one tends to flatten the intra-cavity field, usually quantified by a flatness parameter ($\mathfrak{F}$).

The inclusion of inhomogeneous coupling strengths along standard QWS-DFB structures can be especially attractive in the increase of $\mathfrak{S}$, if the coupling coefficient is made larger in the central zone of the laser corrugation [3, pp. 136–145], [5], [6]. This structure is designated by distributed-coupling-coefficient (DCC)-DFB laser structure and it has been commonly referred in literature [3, pp. 136–145], [4] in the OCS context. Further improvements on $\mathfrak{S}$ may be accomplished when the coupling coefficient profile is smoothed, that is, when some intermediate coupling coefficient sections are inserted between the central and side zones of the cavity [7].

The inclusion of multiple phase-shifts (MPS) along the corrugation flattens the electric field distribution along the cavity, though at the expense of a decrease in the laser mode selectivity [3, pp. 124–135], [8]. Nevertheless, the reduction in the mode discrimination is not so drastic if we consider a distributed phase-shift rather than localized MPS discontinuities. This is accomplished using different grating periods along the laser cavity, which corresponds to the corrugation-pitch-modulated (CPM)-DFB laser structure [4], [9].

The aim of this paper is to propose a suitable and judicious design of a DFB laser that combines the advantages of using laser structures with both smooth inhomo-

geneous coupling coefficient profile and variable grating periods along the cavity [4].

This paper is organised as follows. In section 2, an improved version of the transfer-matrix-method (TMM) is fully described. In section 3, the laser structure under optimisation is presented, optimised and analysed. In section 4, the main conclusions are summarised.

2 The Transfer-Matrix-Method

In order to ensure a quick convergence in the simulation of DFB laser characteristics at threshold and above-threshold regimes, an improved version of the TMM is presented and fully described in this section.

2.1 Threshold Analysis

To perform the TMM-based model analysis for laser threshold, the laser cavity with length L is divided into M concatenated sections, which are identified by the constancy of its structural parameters. For the m-th section with length L_m, those structural parameters are: the corrugation period Λ_m, the amount of feedback per unit length $\overline{\kappa}_m$ and the phase of the section grating with respect to the left side of the cavity Ω_m.

Each section is described by two counter propagating electrical field waves described by their complex amplitudes $\overline{E}_{R}(z)$ and $\overline{E}_{S}(z)$, which allow the internal electrical field intensity $\mathbb{E}(t,z)$, to be determined according to

$$\mathbb{E}(t,z) \propto \Re\left\{ \left[\overline{E}_{R}(z) + \overline{E}_{S}(z)\right] \cdot \exp\left(\jmath\,\omega\, t\right)\right\} \quad , \qquad (1)$$

where t is the time, z is the $z-$axis coordinate, $\Re\{\cdot\}$ is the real part operator, $\jmath = \sqrt{-1}$ and ω is the field angular frequency. Equation (1) assumes that the longitudinal laser axis coincides with the $z-$axis. In the TMM the column matrices related to $\overline{E}_{R}(z)$ and $\overline{E}_{S}(z)$ components are considered for the same spatial position (see Fig. 1).

On the basis of the coupled wave equations [10], the transfer matrix for the m-th section of the one-dimensional DFB laser structure indicated in Fig. 1 is given by [3, p. 105], [4]

$$\mathbf{T}(z_{m+1}/z_m) = \begin{bmatrix} t_{11}^{m)} & t_{12}^{m)} \\ t_{21}^{m)} & t_{22}^{m)} \end{bmatrix} \quad , \qquad (2)$$

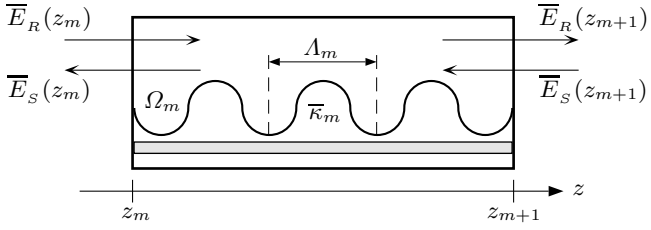

Fig. 1 – A simplified schematic diagram for a one-dimensional DFB laser structure section, placed between $z = z_m$ and $z = z_{m+1}$.

and it links the column matrices related to the complex electric fields of the wave solutions at z_m and z_{m+1}

$$\begin{bmatrix} \overline{E}_{R}(z_{m+1}) \\ \overline{E}_{S}(z_{m+1}) \end{bmatrix} = \mathbf{T}(z_{m+1}/z_m) \cdot \begin{bmatrix} \overline{E}_{R}(z_m) \\ \overline{E}_{S}(z_m) \end{bmatrix} \quad , \qquad (3)$$

where $t_{11}^{m)}$, $t_{12}^{m)}$, $t_{21}^{m)}$ and $t_{22}^{m)}$ are given, respectively, by

$$\begin{aligned} t_{11}^{m)} &= \frac{\xi_m - \overline{\rho}_m^2\ \xi_m^{-1}}{\left(1-\overline{\rho}_m^2\right)\ \zeta_m};\ t_{12}^{m)} = -\frac{\overline{\rho}_m \left(\xi_m - \xi_m^{-1}\right) e^{-\jmath\,\Omega_m}}{\left(1-\overline{\rho}_m^2\right)\ \zeta_m} \\ t_{21}^{m)} &= \frac{\overline{\rho}_m \left(\xi_m - \xi_m^{-1}\right) e^{\jmath\,\Omega_m}}{\left(1-\overline{\rho}_m^2\right)\ \zeta_m^{-1}};\ t_{22}^{m)} = -\frac{\overline{\rho}_m^2\ \xi_m - \xi_m^{-1}}{\left(1-\overline{\rho}_m^2\right) \zeta_m^{-1}} \end{aligned} \qquad (4)$$

with $\xi_m = e^{\overline{\gamma}_m \cdot (z_{m+1} - z_m)}$ and $\zeta_m = e^{\jmath\,\beta_m \cdot (z_{m+1} - z_m)}$. The propagation constant, β_m, and the complex propagation constant, $\overline{\gamma}_m$, are given, respectively, by

$$\beta_m = \frac{\pi}{\Lambda_m} \quad ; \quad \overline{\gamma}_m = \sqrt{\left(\alpha - \jmath\,\delta_m\right)^2 + \overline{\kappa}_m^2} \quad , \qquad (5)$$

where $\overline{\rho}_m$ and δ_m are given by

$$\overline{\rho}_m = \frac{\jmath\,\overline{\kappa}_m}{\alpha - \jmath\,\delta_m + \overline{\gamma}_m} \ ;\ \delta_m = \delta + \pi\left(\frac{1}{\Lambda_1} - \frac{1}{\Lambda_m}\right) \ , \qquad (6)$$

with α and δ being, respectively, the gain and detuning for the propagation modes taking the left section as a reference. Ω_m is given by [4]

$$\Omega_m = \Omega_1 + 2 \cdot \sum_{k=1}^{m-1} \left(\frac{\pi}{\Lambda_k} \cdot L_k\right) \quad ; \quad 2 \le m \le M \quad . \qquad (7)$$

Equations (4)–(7) are a generalisation of the TMM presented in Ref. [3, p. 151] in order to include laser structures with variations in the grating period, as it is the case of CPM-DFB lasers, the analysis of which is the aim of this paper. Indeed, the TMM described in Ref. [3, p. 151] does not include CPM-DFB laser diodes, since the grating period is always made constant along the laser cavity.

The fields at both ends of the cavity are connected by the elementary matrix product

$$\begin{bmatrix} \overline{E}_{R}(L) \\ \overline{E}_{S}(L) \end{bmatrix} = \mathbf{T}^{\mathrm{Total}} \cdot \begin{bmatrix} \overline{E}_{R}(0) \\ \overline{E}_{S}(0) \end{bmatrix} \quad , \qquad (8)$$

where

$$\mathbf{T}^{\mathrm{Total}} = \prod_{m=M}^{1} \mathbf{T}(z_{m+1}/z_m) \quad . \qquad (9)$$

The formulation of the transfer matrices for other modified DFB laser structures is straightforward, as far as

the changes are correctly translated to the matricial formalism. Namely, the inclusion of the PS discontinuity φ, is given by the following matrix [3, p. 106]

$$\begin{bmatrix} e^{\jmath\,\varphi} & 0 \\ 0 & e^{-\jmath\,\varphi} \end{bmatrix} \quad , \tag{10}$$

assuming that the field discontinuity is usually small along the plane of the PS. In this case the matrix (10) should be included in the matrix product $\mathbf{T}^{\text{Total}}$ indicated in the equation (9), at the correspondent z position. In modified DFB structures with axial variations of the coupling coefficient $\overline{\kappa}(z)$, the minimum number of sections to be considered in the TMM should be compatible with the assumption of a constant value for the coupling coefficient in each section.

The oscillation condition corresponds to the vanishing of the incoming waves and it is determined by the following requirement

$$t_{22}^{\text{Total}}(\alpha, \delta) = 0 \quad , \tag{11}$$

where t_{22}^{Total} is the fourth element of the matrix $\mathbf{T}^{\text{Total}}$, given by (9). The solutions are the mode gain, α, and the detuning, δ, and are related to the modes that are allowed to propagate inside the cavity. For the main mode their values are, respectively, the threshold gain, α_{th}, and the threshold detuning, δ_{th}. For a grating with a first-order Bragg diffraction, the mode gain and the detuning can be expressed, respectively, as [3, p. 151]

$$\alpha(z) = \frac{\Gamma\, g(z) - \alpha_{\text{loss}}}{2} \tag{12}$$

and

$$\delta(z) = \frac{2\,\pi}{\lambda}\, n(z) - \frac{2\,\pi\, n_g}{\lambda\, \lambda_B} \cdot (\lambda - \lambda_B) - \frac{\pi}{\Lambda(z)} \quad , \tag{13}$$

where Γ is the optical confinement factor, α_{loss} is the total loss, n is the effective index, λ_B is the Bragg wavelength, λ is the lasing mode wavelength, n_g is the group effective index and g is the material gain, given by [3, p. 151]

$$g(z) = A_0 \cdot (N(z) - N_0) - \\ - A_1 \cdot \left[\lambda - \left(\lambda_0 - A_2\left(N(z) - N_0\right)\right)\right]^2 . \tag{14}$$

In (14), N is the carrier concentration, A_0 is the differential gain, N_0 is the carrier concentration at transparency ($g = 0$), λ_0 is the peak wavelength at transparency and A_1 and A_2 are parameters used in the parabolic model assumed for the material gain. Using the first-order approximation for the effective index n, one obtains [3, p. 151]

$$n(z) = n_0 + \Gamma\, \frac{\partial n}{\partial N}\, N(z) \quad , \tag{15}$$

where n_0 is the effective index at zero carrier injection and $\partial n/\partial N$ is the differential index. The photon concentration (S) and N are coupled together through the steady-state carrier rate equation [3, p. 152]

$$\frac{I}{q\, V_{act}} = A\, N(z) + B\, N^2(z) + C\, N^3(z) + \\ + \frac{v_g\, g(z)\, S(z)}{1 + \varepsilon\, S(z)} \quad , \tag{16}$$

where I is the injection current, q is the modulus of the electron charge, V_{act} is the volume of the active layer, A is the spontaneous emission rate, B is the radiative spontaneous emission coefficient, C is the Auger recombination coefficient, ε is a non-linear coefficient to take into account saturation effects and $v_g = c/n_g$ is the group velocity, with c being the free space velocity.

In an purely index-coupled DFB laser cavity, which happens to be the case considered along this paper, the mutual interaction between the coupled waves $\overline{E}_{_R}(z)$ and $\overline{E}_{_S}(z)$ can be neglected in the rate of total power change [3, p. 59], [11]. Therefore, the local photon density inside the cavity can be expressed as [3, p. 152]

$$S(z) \approx \frac{2\,\varepsilon_{_0}\, n(z)\, n_g\, \lambda}{h\, c} \cdot c_0^2 \left[\left|\overline{E}_{_R}(z)\right|^2 + \left|\overline{E}_{_S}(z)\right|^2\right] \quad , \tag{17}$$

where $\varepsilon_{_0}$ is the free space permittivity, h is the Planck's constant and c_0 a dimensionless coefficient that allows the determination of the total electric field at the above threshold regime, taking into account that the normalization

$$\left|\overline{E}_{_R}(0)\right|^2 + \left|\overline{E}_{_S}(0)\right|^2 = 1 \tag{18}$$

has been imposed. The equation (18) and the boundary conditions imposed at the left facet allow the calculation of the two counter running waves, $\overline{E}_{_R}(z)$ and $\overline{E}_{_S}(z)$, at $z = 0$. The use of the TMM allows the calculation of the longitudinal electric field profile. The output power at the right facet can be determined as [3, p. 152]

$$P = \frac{d\, w}{\Gamma} \cdot v_g \cdot \frac{h\, c}{\lambda} \cdot S(L) \quad , \tag{19}$$

where d and w are the thickness and width of the active layer, respectively.

From the solutions of the oscillation condition (11), α_{th} and δ_{th} are determined. Using equations (12)– (15), the carrier concentration at threshold (N_{th}), the effective index at threshold ($n_{_{th}}$), the threshold wavelength (λ_{th}) and λ_0 are successively evaluated. Threshold current (I_{th}) is obtained from (16), assuming that S is negligible at threshold. Within this assumption, the z dependence described in eqs. (12), (14) and (15) is also neglected. The same assumption is valid for eq. (13), except for CPM structures where a z dependence is included in $\Lambda(z)$.

2.2 Above-Threshold Analysis

In the above-threshold regime, $S(z)$ is high enough to induce important non-uniformities in $N(z)$ and $n(z)$. Despite the SHB effect can be minimised by an adequate design of the DFB structure, the interdependence of $S(z)$,

$N(z)$ and $n(z)$ induces strong longitudinal inhomogeneities that forces the division of each section into several subsections, in order to ensure a correct evaluation of the above-threshold characteristics. According to Ref. [3, p. 153], for a cavity with $L = 500\,\mu\text{m}$, at least a total of $M = 5000$ subsections are needed.

In this paper, the numerical procedure for the above-threshold calculations follows closely the method developed in Refs. [3, p. 149], [4]. However, in order to ensure a quick convergence in the evaluations of the laser characteristics, an adequate strategy is now proposed, which is fully described below.

2.2.1 Lasing mode analysis

For each bias current I, the numerical above-threshold calculations concerning the lasing mode are summarised as follows:

(i) Successive $(G \times G)$ grids are created in the (c_0, λ) plane. The i-th grid is centred at $\left(c_{0_c}^{i)}, \lambda_c^{i)}\right)$ and it is enclosed in the region defined by the limits $c_{0\min}^{i)}$, $c_{0\max}^{i)}$, $\lambda_{\min}^{i)}$ and $\lambda_{\max}^{i)}$. For the initial grid $(i = 1)$ [1]

$$\lambda_c^{1)} = \lambda_{th} \tag{20}$$

$$c_{0_c}^{1)} = \frac{\sqrt{\dfrac{h\,c\,(I - I_{th})}{2\,q\,V_{act}\,v_g\,g_{th}\,\varepsilon_0\,n_{th}\,n_g\,\lambda_{th}}}}{\sqrt{\left|\overline{E}_{R}(0)\right|^2 + \left|\overline{E}_{S}(0)\right|^2}} \tag{21}$$

$$c_{0\min}^{1)} = c_{0_c}^{1)} - \Delta c_0^{1)} \;\;;\;\; c_{0\max}^{1)} = c_{0_c}^{1)} + \Delta c_0^{1)} \tag{22}$$

$$\lambda_{\min}^{1)} = \lambda_c^{1)} - \Delta\lambda^{1)} \;\;;\;\; \lambda_{\max}^{1)} = \lambda_c^{1)} + \Delta\lambda^{1)} \quad , \tag{23}$$

where $\Delta c_0^{1)} \triangleq c_{0_c}^{1)}/10$ and $\Delta\lambda^{1)} \triangleq 0.1\,\text{nm}$ seem adequate for most of the DFB structures, when $G \approx 10$. However, a readjustment of $\Delta c_0^{1)}$ and $\Delta\lambda^{1)}$ may, occasionally, be necessary in order to prevent an eventual convergence towards a local minimum. This is a critical aspect of the proposed analysis, since an inadequate choice would prevent the numerical convergence;

(ii) For each one of the G^2 pairs of the i-th grid $\left(c_{0_k}^{i)}, \lambda_l^{i)}\right)$ with $k\,; l = 1 \ldots G$, the equations (14) – (17) are self-consistently solved, in order to determine the material gain, carrier density, photon density and effective index for each one of the j sub-section, respectively, g_j, N_j, S_j and n_j, with $1 \le j \le M$;

(iii) The equations (12) and (13) are solved in order to determine the lasing mode gain and detuning for the j-th sub-section, respectively, α_j and δ_j. The transfer matrix of the j-th sub-section, $\mathbf{T}\,(z_{j+1}/z_j)$, is then calculated;

(iv) Using the TMM, the two counter-running waves at the output of the j-th sub-section, $\overline{E}_{R_j}$ and $\overline{E}_{S_j}$, are obtained. For the M-th sub-section, the discrepancy found between those values and the laser right facet boundary condition is represented by $\varepsilon_{kl}^{i)}$. This value is evaluated and stored for each pair $\left(c_{0_k}^{i)}, \lambda_l^{i)}\right)$ of the i-th grid. The error associated to the i-th grid is given by $\varepsilon^{i)} = \min\left(\varepsilon_{kl}^{i)}\right)$;

(v) Whenever $\varepsilon^{i)} = \varepsilon^{i-1)}$, the central pair remains the same $\left(c_{0_c}^{i+1)} = c_{0_c}^{i)}, \lambda_c^{i+1)} = \lambda_c^{i)}\right)$, but new limits are required for the next grid. c_0 and λ discretizations should be reduced, for instance: $\Delta c_0^{i+1)} = \Delta c_0^{i)}/10$ and $\Delta\lambda^{i+1)} = \Delta\lambda^{i)}/10$. Whenever $\varepsilon^{i)} < \varepsilon^{i-1)}$, the pair associated with the $\min\left(\varepsilon_{kl}^{i)}\right)$ is chosen as next central pair $\left(c_{0_c}^{i+1)}, \lambda_c^{i+1)}\right)$, while c_0 and λ discretisations remains unchangeable. For $i = 1$, $\varepsilon^{i-1)}$ is taken as the error associated with the central pair $\left(c_{0_c}^{1)}, \lambda_c^{1)}\right)$.

For each one of the G^2 pairs $\left(c_{0_k}^{i+1)}, \lambda_l^{i+1)}\right)$, the steps (i-v) are repeated until $\varepsilon^{i+1)} \le \varepsilon_{\min}$, where $\varepsilon_{\min}$ is a preset error value (less than 10^{-14}, as indicated in Ref. [3, p. 156]).

Since the gain α_j and the detuning δ_j are z-dependent, the lasing characteristics for each biasing current are associated with their mean values along the cavity, given by

$$\alpha_{av}(I) = \frac{1}{M}\sum_{j=1}^{M}\alpha_j(I) \;\;;\;\; \delta_{av}(I) = \frac{1}{M}\sum_{j=1}^{M}\delta_j(I) \quad . \tag{24}$$

Notice that the sequential analysis (i)-(v) assumes a one-mode propagation laser behaviour. This approach is itself a good assumption, since the present analysis focuses on DFB structures that must ensure SLM operation. Otherwise, different strategies must be adopted.

When studying the I influence on the laser characteristics, a considerable CPU time reduction can be achieved if, for each subsequent current, instead of using (20), $\lambda_c^{1)}$ is taken as the solution found in the previous bias current.

2.2.2 Side mode analysis

$S(z)$, $N(z)$ and $n(z)$ profiles are settled for each I by the lasing mode profiles obtained in sub-section 2.2.1. At threshold, these distributions are nearly uniform along the cavity, assuming average values, respectively, 0, N_{th} and n_{th}. The gain mode and detuning associated with the side-mode, at threshold, respectively, α_{side} and δ_1, are settled. In the one-mode approximation the use of the eq. (13)

[1] Notice that, according to (18), $c_{0_c}^{1)}$ is numerically equal to $\sqrt{h\,c\,(I - I_{th})\,/\,(2\,q\,V_{act}\,v_g\,g_{th}\,\varepsilon_0\,n_{th}\,n_g\,\lambda_{th})}$.

leads to

$$\lambda_{\mathcal{R}}\left(\delta_1\right) = \frac{2\,\pi\,\lambda_B\,\left(n_{_{th}} + n_g\right)}{\delta_1\,\lambda_B + 2\,\pi\,n_g + \dfrac{\pi\,\lambda_B}{\Lambda_{av}}} \quad , \tag{25}$$

where Λ_{av} is the average grating period given by

$$\Lambda_{av} = \frac{\sum\limits_{m=1}^{M} L_m \cdot \Lambda_m}{L} \quad . \tag{26}$$

This assumption means that $\lambda_{\mathcal{R}}\left(\delta_1\right)$ would be the threshold wavelength if δ_1 would correspond to the lasing mode. On the other hand, regarding the side-mode gain, eq. (12) imposes that

$$2\,\alpha_{_{\rm side}} = \Gamma\,g_1 - \alpha_{_{\rm loss}} \quad , \tag{27}$$

where g_1 is obtained from (14), making $N(z) = N_{th}$ and $\lambda = \overline{\lambda}_1\left(\alpha_{_{\rm side}}\right)$. This would be the wavelength in the one-mode approach if $\alpha_{_{\rm side}}$ would correspond to the threshold gain. It will be designated by the *side-mode effective wavelength*. Similarly, for the lasing mode, it is obtained

$$2\,\alpha_{th} = \Gamma\,g_{_{th}} - \alpha_{_{\rm loss}} \quad , \tag{28}$$

where $g_{_{th}} = A_0\left(N_{th} - N_0\right)$. Then, from equations (27) and (28), it can be shown that

$$\overline{\lambda}_1\left(\alpha_{_{\rm side}}\right) = \lambda_{th} + j\,\lambda_{\mathcal{I}}\left(\alpha_{_{\rm side}}\right) \quad , \tag{29}$$

where

$$\lambda_{\mathcal{I}}\left(\alpha_{_{\rm side}}\right) = \sqrt{\frac{2\,\left(\alpha_{_{\rm side}} - \alpha_{th}\right)}{A_1\,\Gamma}} \quad . \tag{30}$$

A $(G \times G)$ grid is created in the plane $(\lambda_{\mathcal{I}}, \lambda_{\mathcal{R}})$ in a similar way as done for the plane (c_0, λ), in sub-section 2.2.1. The initial grid is centered in $\left(\lambda^{1)}_{\mathcal{I}_c}, \lambda^{1)}_{\mathcal{R}_c}\right)$, where $\lambda^{1)}_{\mathcal{I}_c}$ and $\lambda^{1)}_{\mathcal{R}_c}$ are given, respectively, by (30) and (25). The limits of the initial grid are defined by $\lambda^{1)}_{\mathcal{I}_c} \pm \Delta\lambda^{1)}_{\mathcal{I}}$ and $\lambda^{1)}_{\mathcal{R}_c} \pm \Delta\lambda^{1)}_{\mathcal{R}}$. $G = 10$, $\Delta\lambda^{1)}_{\mathcal{I}} \approx 0.01\,\text{nm}$ and $\Delta\lambda^{1)}_{\mathcal{R}} \approx 0.1\,\text{nm}$ seem reasonable for most of the DFB structures but, as before, a readjustment may once in a while be necessary to avoid the mode hopping. Usually $\Delta\lambda^{1)}_{\mathcal{I}}$ is one order of magnitude lower than $\Delta\lambda^{1)}_{\mathcal{R}}$ because the difference between the gains associated with different modes is about one order of magnitude lower than the difference between their detunings. Successive $(G \times G)$ grids are defined in the wavelength plane, centering the i-th grid in $\left(\lambda^{i)}_{\mathcal{I}_c}, \lambda^{i)}_{\mathcal{R}_c}\right)$ and enclosing it in the region defined by the limits $\lambda^{i)}_{\mathcal{I}_c} \pm \Delta\lambda^{i)}_{\mathcal{I}}$ and $\lambda^{i)}_{\mathcal{R}_c} \pm \Delta\lambda^{i)}_{\mathcal{R}}$.

Then, for each pair (k, l) of the i-th grid, i.e. $\left(\lambda^{i)}_{\mathcal{I}_k}, \lambda^{i)}_{\mathcal{R}_l}\right)$, the mode gain and detuning for each one of the j $(j = 1, \ldots, M)$ sub-sections of the cavity are obtained for a given current I as, respectively,

$$\alpha^{i)}_{\text{side}_{kl_j}}(I) = \alpha_j(I) + \left(\lambda^{i)}_{\mathcal{I}_k}\right)^2 \frac{A_1\,\Gamma}{2} \quad , \tag{31}$$

$$\delta^{i)}_{\text{side}_{kl_j}}(I) = \frac{2\,\pi}{\lambda^{i)}_{\mathcal{R}_l}}\,n_j(I) - \frac{2\,\pi\,n_g}{\lambda^{i)}_{\mathcal{R}_l}\,\lambda_B} \cdot \left(\lambda^{i)}_{\mathcal{R}_l} - \lambda_B\right) - \frac{\pi}{\Lambda_j} \quad . \tag{32}$$

In eqs. (31) and (32), $\alpha_j(I)$ and $n_j(I)$ are, respectively, the lasing mode gain and the refractive index associated with the j-th sub-section for a biasing current I, achieved in subsection 2.2.1. Besides, Λ_j is the corrugation period of the j-th sub-section.

Similarly as in sub-section 2.2.1, steps (iii)–(v) are then sequentially followed. The side-mode analysis is quicker than the lasing mode analysis since the step (ii) described in sub-section 2.2.1 is not necessary.

Table 1 – Summary of laser parameters

Laser parameter	**Value**
Material parameters	
Spontaneous emission rate, A	$2.5 \times 10^{8}\,\text{s}^{-1}$
Bimolecular recombination coefficient, B	$1.0 \times 10^{-16}\,\text{m}^3 \cdot \text{s}^{-1}$
Auger recombination coefficient, C	$3.0 \times 10^{-41}\,\text{m}^6 \cdot \text{s}^{-1}$
Differential gain, A_0	$2.70 \times 10^{-20}\,\text{m}^2$
Gain curvature, A_1	$1.50 \times 10^{19}\,\text{m}^{-3}$
Differential peak wavelength, A_2	$2.70 \times 10^{-32}\,\text{m}^4$
Internal loss, $\alpha_{_{\rm loss}}$	$4.0 \times 10^{3}\,\text{m}^{-1}$
Effective index at zero injection, n_0	3.41351524
Carrier density at transparency, N_0	$1.23 \times 10^{24}\,\text{m}^{-3}$
Differential index, $\text{d}\,n/\text{d}\,N$	$-1.8 \times 10^{-26}\,\text{m}^3$
Group velocity, v_g	$8.33 \times 10^{7}\,\text{m} \cdot \text{s}^{-1}$
Nonlinear gain coefficient, ε	$1.5 \times 10^{-23}\,\text{m}^3$
Structural parameters	
Active layer width, w	$1.5\,\mu\text{m}$
Active layer thickness, d	$0.12\,\mu\text{m}$
Cavity length, L	$500\,\mu\text{m}$
Optical confinement factor, Γ	0.35

3 The CPM-DCC-DFB Laser

3.1 Structure Description and Parameters Definition

The laser structure under analysis is a CPM-DCC-DFB (see Fig. 2). This is a multi-section anti-reflection (AR)-coated with two grating periods Λ_s and Λ_c, and three coupling coefficients $\overline{k}_s$, $\overline{k}_{sc}$ and $\overline{k}_c$. Their section boundary positions, normalised by L, are defined by $k_{P_{1a}}$, $k_{P_{1b}}$, $k_{P_{2a}}$, $k_{P_{2b}}$, Λ_{P_1} and Λ_{P_2}. A purely index-coupled laser structure, which assures that the coupling coefficients are real [3, pp. 56–57], is assumed, with $L = 500\,\mu\text{m}$, $\Lambda_s = 227.039\,\text{nm}$ and $\Omega_1 = 0\,\text{rad}$. This kind of structures

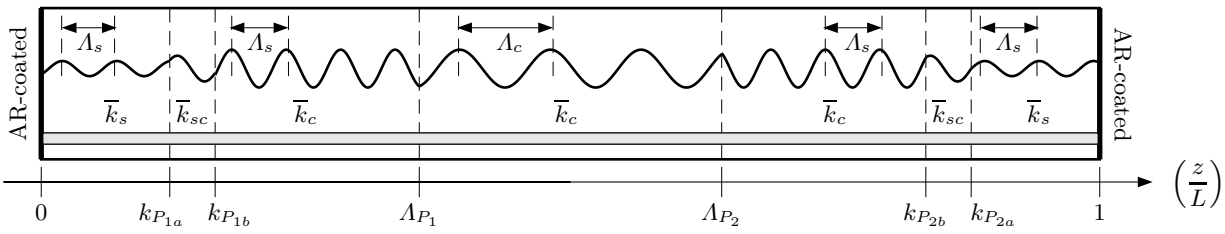

Fig. 2 – A simplified schematic diagram for the CPM-DCC-DFB laser structure.

are generally associated with technological processes that are easier to implement than the gain-coupled structures [1, p. 173], [11], [12]. A symmetric structure is assumed, which means that

$$k_{P_{2a}} = 1 - k_{P_{1a}} \;;\; k_{P_{2b}} = 1 - k_{P_{1b}} \;;\; \Lambda_{P_2} = 1 - \Lambda_{P_1} \quad . \tag{33}$$

The DCC structure is defined by the positions of the discontinuities in the coupling coefficient, $k_{P_{1a}}$, $k_{P_{1b}}$, $k_{P_{2a}}$ and $k_{P_{2b}}$, the value $\overline{k}_{sc}$ and the coupling ratio, described by

$$\overline{\kappa}_{\text{ratio}} = \frac{\overline{k}_c}{\overline{k}_s} \quad , \tag{34}$$

whereas the CPM profile is described by the positions of the discontinuities in the corrugation period, Λ_{P_1} and Λ_{P_2}, and the relative variation in the corrugation period

$$\Delta\Lambda = \frac{\Lambda_c - \Lambda_s}{\Lambda_s} \quad . \tag{35}$$

In order to allow a straightforward comparison with conventional DFB structures (those with constant coupling coefficient), a parameter known as the averaged coupling coefficient, $\overline{\kappa}_{\text{av}}$, is introduced in the CPM-DCC-DFB structure such that

$$\begin{aligned}\overline{\kappa}_{\text{av}} = 2 \cdot \Big[& \overline{k}_s \cdot \left(k_{P_{1a}}\right) + \overline{k}_{sc} \cdot \left(k_{P_{1b}} - k_{P_{1a}}\right) \\ & + \overline{k}_c \cdot \left(0.5 - k_{P_{1b}}\right) \Big] \quad .\end{aligned} \tag{36}$$

The normalised mode selectivity and the flatness of the electric field are given, respectively, by [3, p. 84 and p. 131]

$$\mathfrak{S} = (\alpha_{_2} L) - (\alpha_{_1} L) \quad ; \quad \mathfrak{F} = \frac{1}{L} \int_0^L \left[\mathcal{I}(z) - \overline{\mathcal{I}}\right]^2 \mathrm{d}\, z \tag{37}$$

where $(\alpha_{_1} L)$ is the normalised dominant mode gain and $(\alpha_{_2} L)$ is the normalised gain of the main side mode. Besides, $\mathcal{I}(z)$ is the normalised electric field intensity at an arbitrary position, z, given by[2]

$$\mathcal{I}(z) = \frac{\left|\overline{E}_{_R}(z)\right|^2 + \left|\overline{E}_{_S}(z)\right|^2}{\left|\overline{E}_{_R}(0)\right|^2 + \left|\overline{E}_{_S}(0)\right|^2} \quad , \tag{38}$$

[2] Notice that, according to (18), $\mathcal{I}(z)$ is numerically equal to $\left|\overline{E}_{_R}(z)\right|^2 + \left|\overline{E}_{_S}(z)\right|^2$.

and $\overline{\mathcal{I}}$ is its average value along the cavity. The laser structural and material parameters used along the paper are summarised in Table 1 [3, p. 157].

3.2 Structure Optimisation at Threshold

The objective of the CPM-DCC-DFB laser structure optimisation is, simultaneously, maximize $\mathfrak{S}$ and minimize $\mathfrak{F}$, at threshold, by varying simultaneously and independently the following set of variables (decision variables): $\overline{\kappa}_{\text{ratio}}$, $\overline{\kappa}_{\text{av}} L$, $k_{P_{1a}}$, $k_{P_{1b}}$, Λ_{P_1} and $\Delta\Lambda$. It should be emphasized that $\mathfrak{S}$ is calculated according to the first expression of (37), where $\alpha_{_1} L$ and $\alpha_{_2} L$ are evaluated at threshold. In this situation, $\alpha_{_1} L$ is designated by $\alpha_{th}\, L$.

The optimisation process is divided into two stages and fully described in the following step-by-step procedure. The first stage, which corresponds to Steps 1–3, is performed assuming that $k_{P_{1a}} = k_{P_{1b}}$ and hence $k_{P_{2a}} = k_{P_{2b}}$. In the second stage, which corresponds to Steps 5–6, $k_{P_{1a}} \neq k_{P_{1b}}$ is assumed and hence $k_{P_{2a}} \neq k_{P_{2b}}$.

Initially $\mathfrak{S} \geq 0.25$ $\left(\mathfrak{S}_{\min} = 0.25\right)$ and $\mathfrak{F} \leq 0.05$ $\left(\mathfrak{F}_{\max} = 0.050\right)$ is required, since these limits have been generally accepted as good boundaries in order to reach a stable SLM operation [3, p. 128 and p. 131]. After each step, the selection criteria are adjusted by fixing tighter limits, i.e., higher $\mathfrak{S}_{\min}$ and smaller $\mathfrak{F}_{\max}$. Initially, $\Delta\Lambda = 10^{-3}$, $\overline{\kappa}_{\text{ratio}} = 5$ and $\overline{\kappa}_{\text{av}} L = 2$ are assumed.

Step 1: The optimisation of $\mathfrak{S}\left(\Lambda_{P_1}, k_{P_{1a}}\right)$ and $\mathfrak{F}\left(\Lambda_{P_1}, k_{P_{1a}}\right)$ is performed by varying simultaneously and independently Λ_{P_1} and $k_{P_{1a}}$ in their entire ranges $0 \leq \Lambda_{P_1} \leq 0.5$ and $0 \leq k_{P_{1a}} \leq 0.5$. The conditions $\mathfrak{S}\left(\Lambda_{P_1}, k_{P_{1a}}\right) \geq \mathfrak{S}_{\min}$ and $\mathfrak{F}\left(\Lambda_{P_1}, k_{P_{1a}}\right) \leq \mathfrak{F}_{\max}$ are used as selection criteria. This step leads to the definition of a region in the plane $(\Lambda_{P_1}, k_{P_{1a}})$, from which a solution is chosen and new boundaries $(\mathfrak{S}_{\min}, \mathfrak{F}_{\max})$ are settled;

Step 2: Assuming Λ_{P_1} and $k_{P_{1a}}$ achieved in Step 1, the optimisation of $\mathfrak{S}\left(\Delta\Lambda, \overline{\kappa}_{\text{ratio}}\right)$ and $\mathfrak{F}\left(\Delta\Lambda, \overline{\kappa}_{\text{ratio}}\right)$ is performed by varying simultaneously and independently $\Delta\Lambda$ and $\overline{\kappa}_{\text{ratio}}$ in the ranges $2 \times 10^{-4} \leq \Delta\Lambda \leq 15 \times 10^{-4}$ and $4 \leq \overline{\kappa}_{\text{ratio}} \leq 14$. The conditions $\mathfrak{S}\left(\Delta\Lambda, \overline{\kappa}_{\text{ratio}}\right) \geq \mathfrak{S}_{\min}$ and $\mathfrak{F}\left(\Delta\Lambda, \overline{\kappa}_{\text{ratio}}\right) \leq \mathfrak{F}_{\max}$ are used as selection criteria, where $(\mathfrak{S}_{\min}, \mathfrak{F}_{\max})$ are the boundaries settled in Step 1. New boundaries $(\mathfrak{S}_{\min}, \mathfrak{F}_{\max})$ are now defined;

Step 3 Assuming the laser structure defined at the end of Step 2, the optimisation of $\mathfrak{S}\left(\overline{\kappa}_{\text{av}} L\right)$ and $\mathfrak{F}\left(\overline{\kappa}_{\text{av}} L\right)$ is

performed by varying $\overline{\kappa}_{\text{av}}\,L$ in the range $0.5 \leq \overline{\kappa}_{\text{av}}\,L \leq 3.5$. The conditions $\mathfrak{S}\left(\overline{\kappa}_{\text{av}}\,L\right) \geq \mathfrak{S}_{\min}$ and $\mathfrak{F}\left(\overline{\kappa}_{\text{av}}\,L\right) \leq \mathfrak{F}_{\max}$ are used as selection criteria, where $(\mathfrak{S}_{\min}, \mathfrak{F}_{\max})$ are the boundaries settled in Step 2. New boundaries $(\mathfrak{S}_{\min}, \mathfrak{F}_{\max})$ are now defined;

Step 4: Steps 1-2-3 are repeated until no improvements on $\mathfrak{S}$ and $\mathfrak{F}$ are achieved.

Step 5: It is assumed that $k_{P_{1a}}$ and $k_{P_{1b}}$ are no longer the same, so that extra intermediate cavity subsections with coupling coefficient $\overline{k}_{sc}$ and grating period Λ_s (see Fig. 2) are introduced. It is imposed that $\overline{k}_{sc} = \overline{k}_s \cdot \sqrt{\overline{\kappa}_{\text{ratio}}}$, considering the $\overline{\kappa}_{\text{ratio}}$ settled in Step 2. The other structural parameters are those settled at the end of Step 4;

Step 6: The optimisation of $\mathfrak{S}\left(k_{P_{1a}}, k_{P_{1b}}\right)$ and $\mathfrak{F}\left(k_{P_{1a}}, k_{P_{1b}}\right)$ is performed assuming the structure defined in Step 5, by varying simultaneously and independently $k_{P_{1a}}$ and $k_{P_{1b}}$. The conditions $\mathfrak{S}\left(k_{P_{1a}}, k_{P_{1b}}\right) \geq \mathfrak{S}_{\min}$ and $\mathfrak{F}\left(k_{P_{1a}}, k_{P_{1b}}\right) \leq \mathfrak{F}_{\max}$ are used as selection criteria, where $(\mathfrak{S}_{\min}, \mathfrak{F}_{\max})$ are the boundaries settled in Step 4. This step leads to the definition of a region in the plane $(k_{P_{1a}}, k_{P_{1b}})$, from which a solution is chosen.

At the final of Step 6, the optimised symmetric CPM-DCC-DFB laser structure is defined by $\{\overline{\kappa}_{\text{ratio}}, (\overline{\kappa}_{\text{av}}\,L), k_{P_{1a}}, k_{P_{1b}}, \Lambda_{P_1} \text{and } \Delta\Lambda\}$, corresponding to the optima values for $\mathfrak{S}$ and $\mathfrak{F}$.

Fig. 3 shows the contour maps for $\mathfrak{S}\left(\Lambda_{P_1}, k_{P_{1a}}\right)$ and $\mathfrak{F}\left(\Lambda_{P_1}, k_{P_{1a}}\right)$, assuming $\overline{\kappa}_{\text{av}}\,L = 1.7$, $\overline{\kappa}_{\text{ratio}} = 8.5$ and $\Delta\Lambda = 9.5000 \times 10^{-4}$. This figure corresponds to an intermediate iteration of Step 1 for the structure optimisation. Solid lines enclose all combinations Λ_{P_1} and $k_{P_{1a}}$ that ensure $\mathfrak{S}\left(\Lambda_{P_1}, k_{P_{1a}}\right) \geq \mathfrak{S}_{\min}$ and $\mathfrak{F}\left(\Lambda_{P_1}, k_{P_{1a}}\right) \leq \mathfrak{F}_{\max}$, where $\mathfrak{S}_{\min} = 1.6$ and $\mathfrak{F}_{\max} = 0.03$ have been settled in the previous iteration. The chosen solution for the next iteration is $\Lambda_{P_1} = 0.3986$ and $k_{P_{1a}} = 0.1986$ (marked $\times$), which corresponds to $\mathfrak{S} = 2.11$ and $\mathfrak{F} = 0.018$.

At the end of the structure optimisation process, the final solution has been found and it is summarised in Table 2.

Table 2 – Laser structure parameters for the optimised CPM-DCC-DFB.

Parameter	Symmetric CPM-DCC
$\overline{\kappa}_{\text{ratio}}$	10.0
$\overline{\kappa}_{\text{av}}\,L$	1.7
$k_{P_{1a}}$	0.1578
$k_{P_{1b}}$	0.2362
Λ_{P_1}	0.4014
$\Delta\Lambda$	9.8571×10^{-4}

According to expressions (34) – (36), this solution corresponds to a CPM-DCC-DFB structure (see Fig. 2)

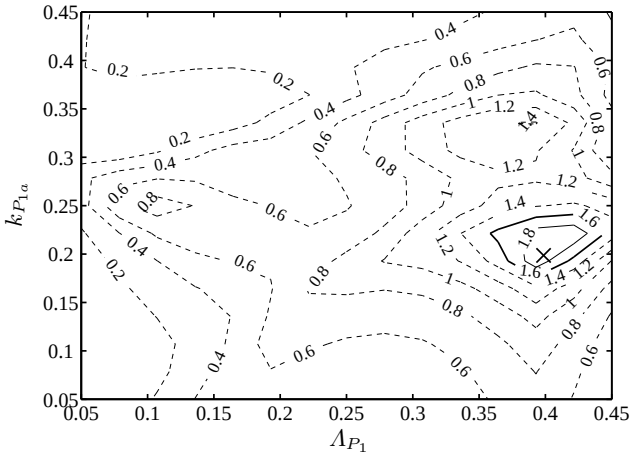

(a)

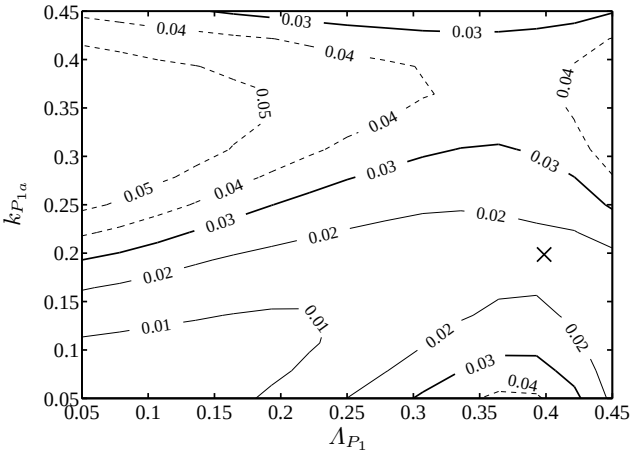

(b)

Fig. 3 – (a) $\mathfrak{S}(\Lambda_{P_1}, k_{P_{1a}})$ and (b) $\mathfrak{F}(\Lambda_{P_1}, k_{P_{1a}})$, assuming $\overline{\kappa}_{\text{av}}\,L = 1.7$, $\overline{\kappa}_{\text{ratio}} = 8.5$ and $\Delta\Lambda = 9.5000 \times 10^{-4}$. Values for $\mathfrak{S} \geq \mathfrak{S}_{\min}$ and $\mathfrak{F} \leq \mathfrak{F}_{\max}$ are represented by a solid line. $\mathfrak{S}_{\min} = 1.6$ and $\mathfrak{F}_{\max} = 0.03$ are considered.
($\times$ solution: $\Lambda_{P_1} = 0.3986$ and $k_{P_{1a}} = 0.1986$, which corresponds to $\mathfrak{S} = 2.11$ and $\mathfrak{F} = 0.018$)

where: $\overline{k}_s L = 0.28$, $\overline{k}_{sc} L = 0.88$, $\overline{k}_c L = 2.79$ and $\Lambda_c = 227.263\,\text{nm}$. This structure has $\mathfrak{S} = 2.54$, $\mathfrak{F} = 0.019$ and $\alpha_{th}\,L = 1.48$, corresponding to $I_{th} = 25.766\,\text{mA}$.

Table 3 summarises the results for $\mathfrak{S}$, $\mathfrak{F}$ and $\alpha_{th}\,L$ achieved for three different laser structures: the QWS-DFB, the CPM-DCC-DFB from [4], indicated as a possible optimum design for CPM-DCC-DFB laser structures, and the optimised CPM-DCC-DFB proposed in this paper.

It is worth noticing that the optimised CPM-DCC-DFB laser structure proposed in this paper is clearly advantageous. In fact, it is the structure with the highest $\mathfrak{S}$, which is 2.5 times greater than the one related to the CPM-DCC-DFB laser structure proposed in Ref. [4], revealing outstanding performance. Moreover,

Table 3 – $\mathfrak{S}$, $\mathfrak{F}$ and $\alpha_{th}\,L$ for several laser structures. $\overline{\kappa}\,L = 2.0$ is assumed for the 1st structure. $\overline{\kappa}\,L = 2.06$ is assumed for the 2nd structure. $\overline{\kappa}\,L = 1.7$ is assumed for the 3rd structure.

Laser structure	$\mathfrak{S}$	$\mathfrak{F}$	$\alpha_{th}\,L$
QWS-DFB	0.73	0.301	0.70
CPM-DCC-DFB from [4]	0.99	0.019	1.28
Opt. CPM-DCC-DFB	2.54	0.019	1.48

its $\mathfrak{F}$ is roughly fifteen times better than the one reported for the QWS-DFB. This improvement is achieved at the expense of an increase in the threshold gain which can be overcome by a suitable design of the transversal laser structure [1], [2].

3.3 Above-Threshold Performance

A threshold analysis for the the optimised CPM-DCC-DFB structure has been presented. Nevertheless, even if a structure presents an adequate performance at threshold, an above-threshold analysis is essential in order to assess the rate at which the SHB deteriorates the laser features with the increasing current.

The $S(z)$ distribution in the optimised symmetric CPM-DCC-DFB laser cavity can be observed in Fig. 4, as well as the $N(z)$ distribution, both for $I/I_{th} = 4$. This figure clearly illustrates the SHB effect: an high value of $S(z)$ is achieved at the expense of a reduction of $N(z)$ and vice-versa.

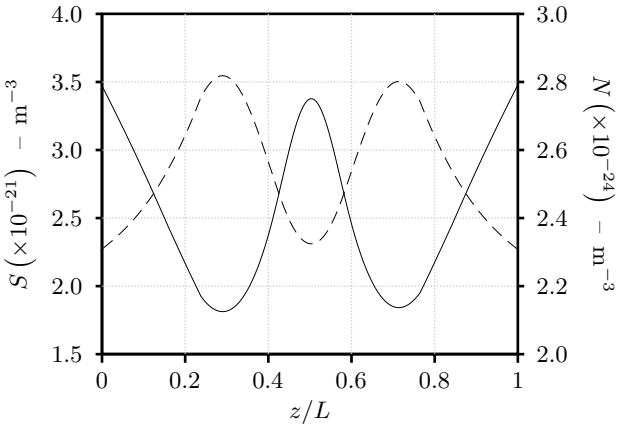

Fig. 4 – Longitudinal distribution of the $S(z)$ (solid) and $N(z)$ (dashed) in the CPM-DCC-DFB laser for $I/I_{th} = 4$.

A comparative analysis between the standard QWS-DFB laser, the CPM-DCC-DFB laser from Ref. [4] and the optimised CPM-DCC-DFB laser presented in this paper is available in Figs. 5– 10.

Fig. 5 shows the laser mode selectivity *vs* normalised current injection. Concerning the mode gain discrimination, the optimised CPM-DCC-DFB laser is, undoubtedly, the best option given that it has the highest $\mathfrak{S}$ values. This figure also shows that $\mathfrak{S}$ presents a significant reduction with increasing biasing current, for the QWS-DFB laser and the CPM-DCC-DFB laser of Ref [4], showing that these lasers are strongly affected by the SHB effect. On the contrary, the optimised CPM-DCC-DFB laser proposed in this paper shows a general increase of $\mathfrak{S}$ with the current injection.

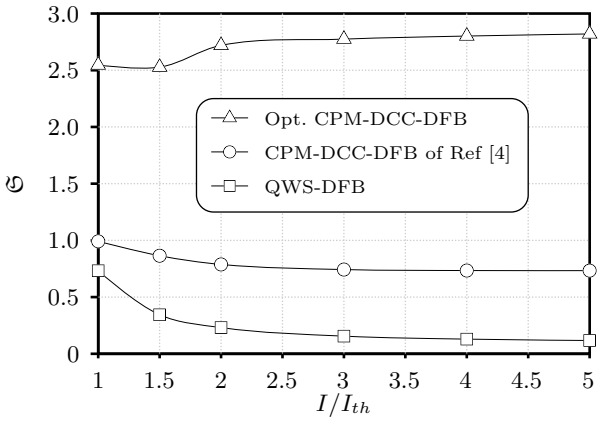

Fig. 5 – Selectivity *vs* normalised current injection for the optimised CPM-DCC-DFB laser, the CPM-DCC-DFB laser of Ref [4] and the standard QWS laser with $L = 500\,\mu$m.

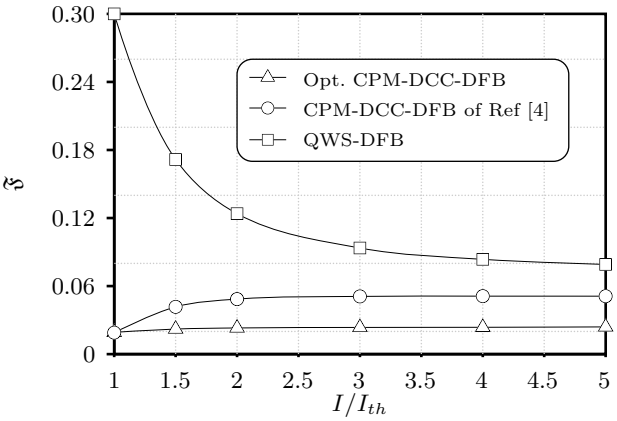

Fig. 6 – Flatness *vs* normalised current injection for the optimised CPM-DCC-DFB laser, the CPM-DCC-DFB laser of Ref [4] and the standard QWS laser with $L = 500\,\mu$m.

Fig. 6 focuses on the evolution of the flatness with the current injection. This figure demonstrates that the optimised CPM-DCC-DFB proposed in this paper is the only one that fulfils the selection criteria commonly referred for lasers with 500 µm cavity length ($\mathfrak{F} \leq 0.05$) [3, p. 131], throughout the entire biasing current range. The associated $\mathfrak{F}$ has a very low and nearly constant value of about 0.019 under the current range under analysis.

The gathering of results from Figs. 5 and 6 undoubtedly demonstrates the high immunity of the optimised CPM-DCC-DFB laser proposed in this paper to the SHB effect. These results show that an adequate profile design

for this laser revealed crucial for the improvement of laser performance in the high power regime.

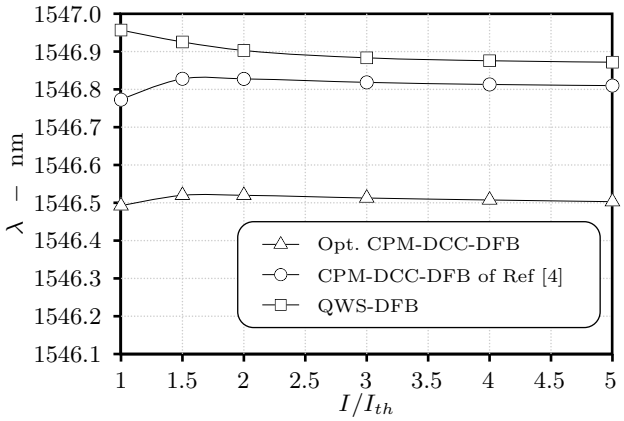

Fig. 7 – Lasing wavelength *vs* current injection for the optimised CPM-DCC-DFB laser, the CPM-DCC-DFB laser of Ref [4] and the standard QWS laser with $L = 500\,\mu\text{m}$.

Fig. 7 summarises the results obtained for the lasing wavelength *vs* the normalised current injection for the optimised CPM-DCC-DFB laser, the CPM-DCC-DFB laser of Ref [4] and the standard QWS laser. The three lasers are associated with stable outputs, foreseeing their potential use as optical carriers as far as lasing wavelength stability is concerned. However, these results show than in the range $1 \leq I/I_{th} \leq 5$ the optimised CPM-DCC-DFB laser presented in this paper outperforms the other two lasers under analysis. In fact, it shows a lasing wavelength relative variation $\Delta\lambda/\lambda_{th} = 1.9 \times 10^{-5}\,\%$, which is lower than the values achieved for the CPM-DCC-DFB laser from Ref. [4] and the QWS-DFB laser, of respectively, $3.6 \times 10^{-5}\,\%$ and $5.5 \times 10^{-5}\,\%$.

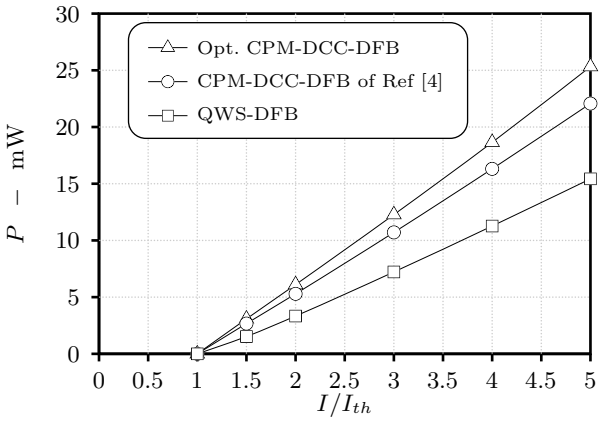

Fig. 8 – Emitted power *vs* current injection for the optimised CPM-DCC-DFB laser, the CPM-DCC-DFB laser of Ref [4] and the standard QWS laser with $L = 500\,\mu\text{m}$.

Fig. 8 shows the light-current stationary characteristic for the three lasers under analysis. For similar normalised current injections, the optimised CPM-DCC-DFB laser proposed in this paper shows larger values for the optical power output (measured at the right facet). Moreover, it has been checked that the optimised CPM-DCC-DFB laser proposed in this paper has the highest external differential efficiency.

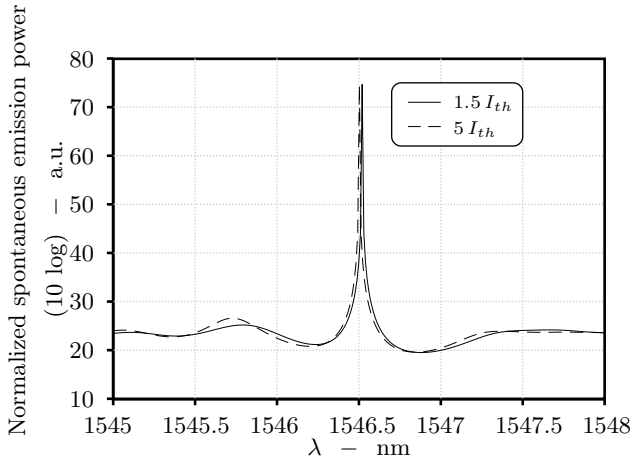

Fig. 9 – Above-threshold normalised spontaneous emission spectra under two different biasing currents for the optimised CPM-DCC-DFB.

The measurement of the laser spectral characteristics is a way of checking its single mode stability. Fig. 9 shows the normalised spontaneous emission power for $I = 1.5\,I_{th}$ and $I = 5\,I_{th}$, for the optimised CPM-DCC-DFB laser. High values of SMSR are achieved, for both bias currents. Besides, it is worth noticing that the "blue-shift" in wavelength is negligible, which was already noted in Fig. 7, with an almost steady emission wavelength.

Another relevant aspect lies with the fact that, near 1546.5 nm, the spectral amplitude of the dominant mode remains at a high value with the current injection, showing no severe mode competition in the high power regime. This is pin-pointed in Fig. 10, where the SMSR of the optimised DFB laser is maintained throughout the range of biasing current under analysis, above 48 dB, which fulfils the usually required criterium SMSR $\geq 45\,\text{dB}$ for the use of DFB lasers in the OCS context [13, p. 215], contrarily to the other two lasers under analysis.

Finally, it should be stressed that in the optimisation process a symmetric structure has been imposed by the conditions expressed in the eqs. (33). In fact, without this constraint, many other structure solutions might be possible, ensuring high values of $\mathfrak{S}$ and low values of $\mathfrak{F}$. However, asymmetric DCC structures with high values of $\overline{\kappa}_{\text{ratio}}$ present a kink in the light-current and wavelength-current characteristics [14, p. 164] due to the hopping between two possible lasing modes, which impairs its use in the OCS context. This would be the case if the structure optimisation process performed in subsection 3.1 had not taken into account the restrictions (33). Fig. 11 shows the emitted power and lasing wavelength *vs* normalised current injection for an asymmetric CPM-DCC-DFB laser structure resulting from an optimisation which ignored the restric-

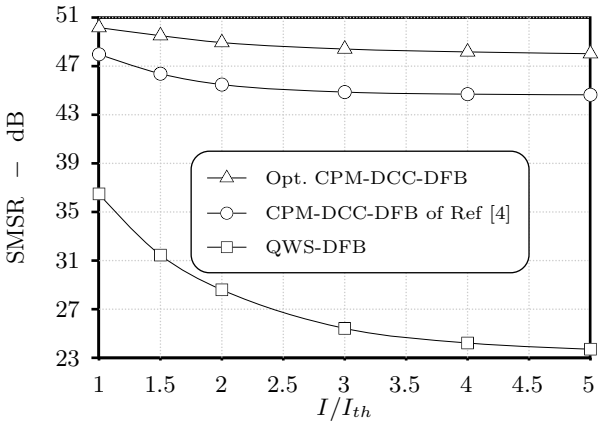

Fig. 10 – Side-mode suppression ration *vs* current injection for the optimised CPM-DCC-DFB laser, the the CPM-DCC-DFB laser of Ref [4] and the QWS-DFB laser with $L = 500\,\mu\text{m}$.

tions (33), which clearly shows the kinks previously referred.

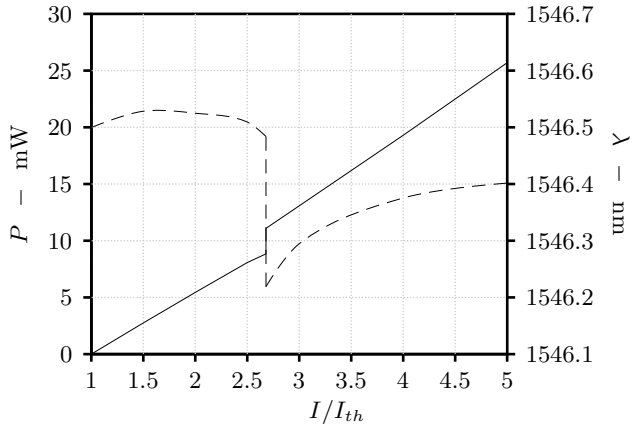

Fig. 11 – Emitted power (solid line) and lasing wavelength (dashed line) *vs* normalised current injection for an asymmetric CPM-DCC-DFB laser structure resulting from an optimisation which ignored the restrictions (33).

4 Conclusions

A symmetric CPM-DCC-DFB laser structure, specially designed to provide SLM operation, has been proposed. An in-depth optimisation of the cavity profile, at threshold, lead to a suitable structure with a three-step coupling coefficient profile and a distributed phase-shift, which ensures the best mode gain margin with flattened intracavity field intensity profile, at threshold.

An above-threshold regime analysis of this CPM-DCC-DFB laser has been carried out, using the TMM and carrier rate equations. In order to accomplish this task, new adequate strategies for efficient TMM convergence above threshold, both for the lasing and the side-modes, have been proposed and fully described along the text. A comparative analysis between the optimised CPM-DCC-DFB laser, the standard QWS-DFB laser and an optimised CPM-DCC-DFB laser referred in Ref. [4] has been performed. This analysis outstands the performance of the proposed structure in the high-power regime. For $I = 5\,I_{th}$, substantial improvements in $\mathfrak{S}$ (3.8 times better), in $\mathfrak{F}$ (2 times better), in P (15 % higher) and in the SMSR (about 3.4 dB higher) are achieved when compared with the laser structure reported in Ref. [4]. This is especially significant in the high bit-rate OCS context, where high biasing currents are demanded in order to ensure high laser bandwidths without a strong degradation due to the SHB effect.

References

1. G. Morthier, P. Vankwikelberge, *Handbook of Distributed Feedback Laser Diodes* (Artech House, Norwood, USA, 1997)
2. G. Agrawal, N. Dutta, *Semiconductor Lasers* (Van Nostrand Reinhold, New York, USA, 1993)
3. H. Ghafouri-Shiraz, *Distributed Feedback Laser Diodes and Optical Tunable Filters* (J. Wiley & Sons, Chich., UK, 2003)
4. T. Fessant, IEE Proc. Optoelectron.– Pt. J **144**(6), 365 (1997)
5. B. Lo, H. Ghafouri-Shiraz, IEEE/OSA J. Lightwave Technol. **13**(2), 200 (1995)
6. S. Nilsson, T. Kjellberg, T. Klinga, J. Wallin, K. Streubel, R. Schatz, IEEE Photon. Technol. Lett. **5**(10), 1128 (1993)
7. T. Fessant, Appl. Phys. B (67), 769 (1998)
8. S. Ogita, Y. Kotaki, M. Matsuda, Y. Kuwahara, H. Ishikawa, IEEE/OSA J. Lightwave Technol. **25**(10), 629 (1989)
9. Y. Dai, J. Yao, IEEE J. Quantum Electron. **44**(10), 938 (2008)
10. H. Kogelnik, C. Shank, J. Appl. Phys. **43**(5), 2327 (1972)
11. E. Kapon, A. Hardy, A. Katzir, IEEE J. Quantum Electron. **18**(1), 66 (1982)
12. K. David, J. Buus, R.G. Baets, IEEE J. Quantum Electron. **28**(2), 427 (1992)
13. T. Shuara, *Semiconductor Laser Fundamentals* (Marcel Dekker, New York, USA, 2004)
14. M. Fukuda, *Optical Semiconducor Devices*, 1st edn. (John Wiley, New York, USA, 1998)